Nonlinear growth of the converging Richtmyer-Meshkov instability in a conventional shock tube

Marc Vandenboomgaerde, Pascal Rouzier, and Denis Souffland
CEA, DAM, DIF, F-91297 Arpajon, France

Laurent Biamino, Georges Jourdan, Lazhar Houas, and Christian Mariani
Aix Marseille Univ, CNRS, IUSTI, Marseille, France

(Received 27 July 2017; published 12 January 2018)

In convergent geometry, the Bell-Plesset (BP) effects modify the growth of hydrodynamic instability in comparison with the planar geometry. They account for acceleration, convergence of the flow, and compressibility of the fluids. To study these effects, the Richtmyer-Meshkov (RM) instability is examined in cylindrical geometry through shock tube experiments. To ease comparisons with models, the canonical single-mode sinusoidal perturbation at the gas interface is considered. The experimental results display a linear time-dependent growth of the amplitude of the instability. First, by cross-checking experiments and numerical simulations with the Hesione code, this peculiar growth for convergent geometry is confirmed. Second, we theoretically explain these results. We derive a new model for the growth of the perturbation in the linear regime of the instability for compressible fluids. Then, it is used to initiate a weakly nonlinear model. This model demonstrates that the linear time-dependent growth of the studied RM instability is due to the nonlinear saturation of the destabilizing BP effects at the interface. This study indicates the importance of taking into account even a slight deceleration of the interface and the compressibility of fluids by correctly describing the background velocity field, which is generated by converging shock waves.

DOI: 10.1103/PhysRevFluids.3.014001

I. INTRODUCTION

Converging shock waves are involved in several fields of high-energy physics, such as astrophysics and inertial confinement fusion (ICF). As their strength increases with time, the focusing shock waves can efficiently heat and compress matter. In the wake of these shock waves, the matter implodes and further compresses. However, the efficiency of this compression can be tempered if the symmetry of the flow is broken. The Richtmyer-Meshkov (RM) hydrodynamic instabilities [1,2] can disrupt this symmetry. It is induced by the passage of a shock wave through a density gradient. For example, in ICF experiments, such gradient occurs at the interface between the deuterium-tritium (DT) core and the encapsulating spherical plastic shell. In these experiments, a specific sequence of converging shock waves is launched to compress the DT fuel. If defects are present at the DT-plastic interface, the RM instability will be triggered. The amplitudes of the defects increase, and it could lead to mixing between the core and the plastic. A mixing zone expanding at the periphery of the DT fuel would dampen the nuclear reactions within the core. Control of the RM instabilities is crucial to ICF success, and reliable models that predict the growth of the RM instabilities in convergent geometries are needed.

In the past few decades, the RM instability was extensively studied in planar geometry. Numerous models have been derived to describe the linear and the nonlinear regimes of the instability for compressible and incompressible flows. Their reliability has been assessed by comparison with several experiments that were often performed in planar shock tubes. In convergent geometry, the growth of the RM instability should be modified. The instability of the interface can first undergo

acceleration or deceleration, which leads to the Rayleigh-Taylor (RT) instability [3,4]. Furthermore, the effects of compression and geometrical convergence must also be taken into account. The discrepancies between the planar RM or RT instability and the convergent case are referred to as the Bell-Plesset (BP) effects [5,6]. To test the corresponding theories and numerical simulations, experimental results with controlled initial conditions are needed. Such experiments in shock tubes are scarce [7]. More data is available with laser experiments [8–11], but these experiments are extremely elaborate [12,13] and require heavy facilities [14–16]. Furthermore, high-energy physics must be taken into account to explain the experimental data [17]. Some models have been derived to study the RM instability in convergent geometry for the canonical problem of a single-mode sinusoidal perturbation between two perfect gases [18–22]. They do not take into account plasma, radiation, thermal transport, or ablation physics. Nonetheless, simple models are an essential step to assess the BP effects. Furthermore, nonlinear theories are also needed [23] and must be tested in the case of a convergent geometry.

Since 2014, we have been building a new shock tube facility [24,25] that generates cylindrical RM instabilities. We study this instability at the interface between gases (SF_6 and air), which are separated by a single-mode sinusoidal interface. This shock tube is derived from a conventional planar shock tube by using the gas lens technique [26]. This technique turns a planar shock wave into a convergent one through the impedance mismatch at a first shaped interface. The resulting shock wave is then guided toward a second interface where the RM instability is studied. The interfaces between gases are materialized by thin nitrocellulosic membranes, which are held on shaped stereolithographed grids.

The purpose of this paper is to analyze the BP effects when the growth of the perturbation is triggered by the RM instability, and the background flow is generated by a converging shock wave. This study is based on experiments that are performed with a convergent shock tube. The shape of the interface between SF_6 and air is a single-mode sinusoid. The first step of our analysis is to fully comprehend the experimental data and to disentangle the side effects due to the apparatus [27,28] from the BP effects. Once the latter are experimentally and numerically quantified, the second step of our analysis is to compare the growth of the perturbation to theoretical models to evaluate the separated influences of the convergence, the compressibility, and the nonlinearity.

The paper is organized as follows. In Sec. II, we present the experimental set-up. In Sec. III, the one-dimensional (1D) flows are discussed. This leads us to specify the actual composition of the involved gases. In Sec. IV, we compare the experimental and numerical shapes of the interface where the RM instability takes place. We explain why the imprint due to the grid bars on the initial shape of the interface must be taken into account. The different features of the experimental data are specified. In Sec. V, we quantify the growth of the instability. We show that the interface is not purely coasting after the shock passage, and it undergoes a slight deceleration before being shocked again (reshock). As a consequence, the BP effects come fully into play. Experimental and numerical peak-to-valley amplitudes are compared, and they are consistent. A theoretical analysis is presented, and we demonstrate that the growth of the instability does not saturate in the nonlinear regime as it would have in the planar case.

II. EXPERIMENTAL SET-UP

The experimental part of this investigation was carried out using a conventional shock tube in horizontal orientation, which has a total length of 3.75 m and a square inner cross section of 80 mm by 80 mm. Details regarding this shock tube can be found in Ref. [29]. At the shock tube end-wall, a specific wedge test section was designed, manufactured, and installed. It has a half apex angle, θ_0, of 15 degrees, and accommodates a three-fluid three-zone system: a test cell of a heavy gas (SF_6) enclosed by light gas (air) on each side as shown in Fig. 1. The shock tube is initially at the atmospheric pressure. The initial expected densities are $\rho_{\text{air}} = 1.204\,\text{kg/m}^3$, and $\rho_{\text{SF6}} = 6.073\,\text{kg/m}^3$. The corresponding adiabatic exponents are $\gamma_{\text{air}} = 1.4$, and $\gamma_{\text{SF6}} = 1.09$. The first air-$SF_6$ interface forms the gas lens which converts a planar shock wave into a cylindrical one. The same configuration (air-SF_6, light-to-heavy case) successfully validated in previous experiments

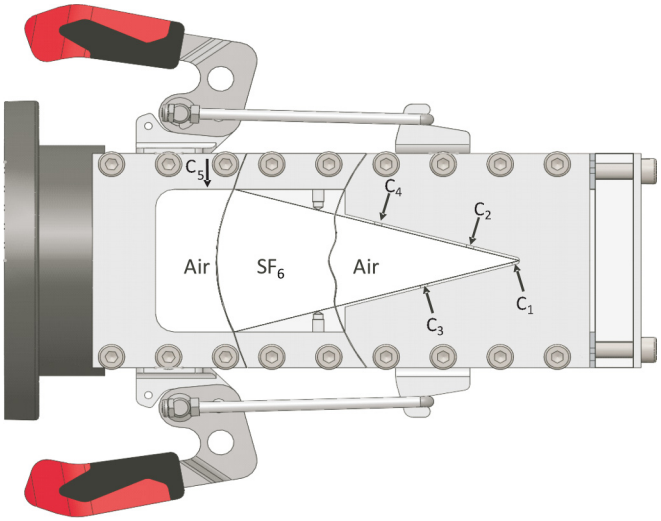

FIG. 1. Scheme of the experimental device adapted on the conventional shock tube and locations of the pressure gauges.

[24] is used again: the incident planar shock wave propagates with a Mach number of 1.15 in air and refracts through an elliptic interface whose polar equation writes as

$$r(\theta) = r(0)\frac{1-e}{1-e\cos(\theta)}, \tag{1}$$

where $e = W_t/W_i$ represents the ratio of the transmitted and incident shock wave velocities, and $r(0) = 0.159$ m is the location of the interface from the apex. The second interface (SF_6-air heavy-to-light case), located at 0.1 m from the apex, presents a single mode perturbation with the following polar equation:

$$r(\theta) = 0.1 - 0.0015\left[1 - \cos\left(\frac{2\pi\theta}{\theta_0}\right)\right], \tag{2}$$

with $\theta_0 = \arctan(\frac{0.04}{0.15})$. The materialization of the interfaces was obtained by a 0.5-μm-thick double layer of nitrocellulose membrane combined with a grid. The first and second interfaces are held by a 8×9.5 mm^2, and 12.85×16 mm^2 mesh grid, respectively. These grids are obtained by stereolithography [30]. This technique enables precise shapes for the grid, i.e., the bars are curved in the azimuthal direction, following Eqs. (1) and (2). The incident shock wave Mach number was experimentally deduced from piezoelectric pressure sensors (Model PCB 113B26) located at two different stations along the shock tube-driven section. The convergent test section was also equipped with five piezoresistive pressure transducers (Model Endevco 8530B), as shown in Fig. 1, which are connected to a multichannel digital oscilloscope (Tektronix DPO4054) through PCN amplifiers (482A22 type). The Schlieren system used here is a standard Z-type Schlieren setup with two concave mirrors on either side of the test section. A 400W Tungsten lamp (from a Dedolight Daylight HMI Spotlight) combined with a condenser is used as a bright white source of light. The light is passed through a horizontal slit (5 mm width), which is placed at the focal point of the first mirror such that the reflected light from the mirror forms parallel rays that pass through the test section. The parallel rays are collected by the second mirror and focused to its focal point at a knife edge. The rays continue on to a Photron Fastcam SA1 high-speed digital camera. The light source is a continuous-wave (CW) light not well suited for short-duration use. However, with the camera having an electronic shutter operating independently of the frame rate selected, it is possible to impose an exposure time of

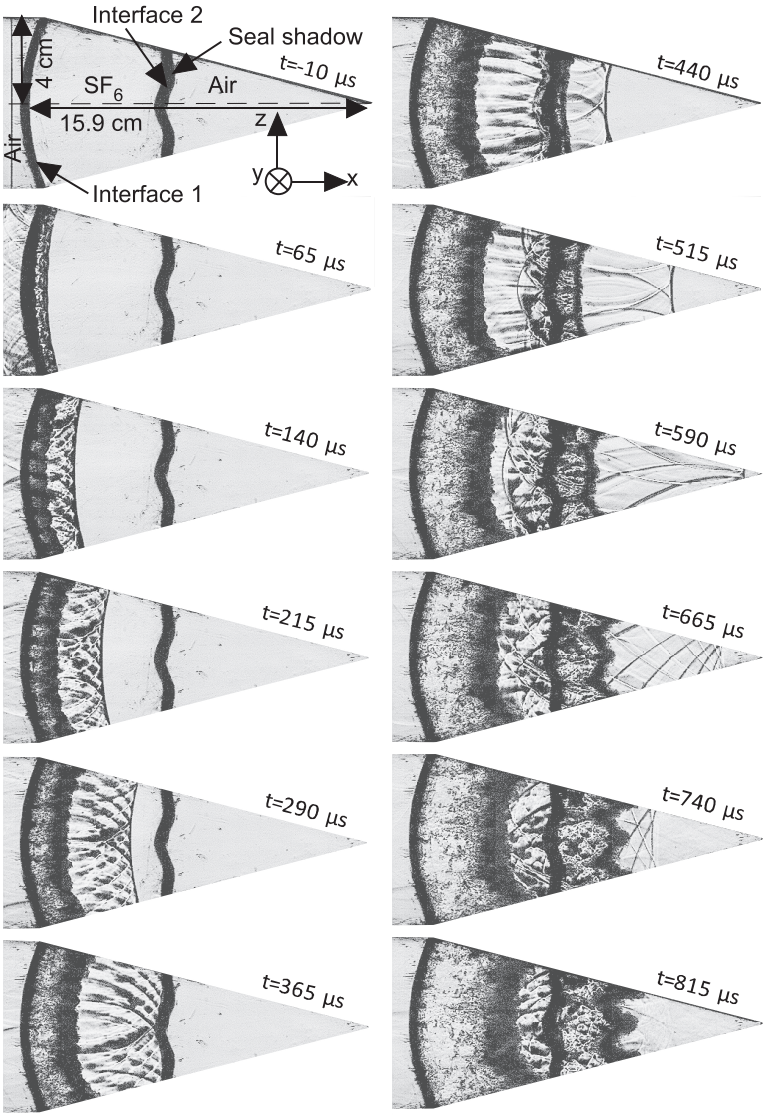

FIG. 2. Sequence of Schlieren pictures (from run #961) showing the evolution of the converging Richtmyer-Meshkov instability at the SF_6-air interface initially materialized by a grid support (12.85×16 mm^2) sandwiched between two layers of 0.5-μm-thick nitrocellulose membrane.

1/1 000 000 s, and to minimize the motion blur. The flow field was monitored with a frame rate of 40 000 frames per second (fps) and a spatial resolution of 512×256 pixels, which corresponds approximatively to 0.625 mm/pix.

In the following, we will discuss results obtained from the Schlieren pictures (Fig. 2). The shock wave moves from left to right and propagates through the three zones (air-SF_6-air). Let us define the origin of times as the moment when the planar shock wave hits the gas lens interface (interface 1). At $t = -10$ μs, the planar shock wave is clearly visible on the left side in the vicinity of the gas lens. When the incident shock wave collides with the air-SF_6 interface, it bifurcates into a transmitted converging cylindrical shock wave, which moves in the central zone from $t = 65$ μs to $t = 365$ μs. At $t = 365$ μs, the converging shock wave impacts the sinusoidally perturbed SF_6-air interface, and

the subsequent pictures (from $t = 440\ \mu$s to $t = 815\ \mu$s) show the different stages of the converging RM instability. As the shock wave hits the interfaces, the nitrocellulose membranes are broken into small pieces. These remnants stay in the vicinity of the interfaces and are seen as a foamy opaque zone in the Schlieren pictures. At this second interface, the converging shock refracts from the heavy fluid (SF_6) to the light one (air). Thus, a phase inversion of the perturbation at the interface occurs. It is completed at $t = 515\ \mu$s. We can also note the geometrical distortion of the shock during its refraction at $t = 440\ \mu$s. It later stabilizes and recovers its cylindrical shape. The horizontal waves behind the moving interface are the consequence of the support grid. Reaching the apex approximatively at $t = 590\ \mu$s, the converging shock wave is reflected back and expands through the evolving SF_6/air interface at $t = 815\ \mu$s.

III. MONODIMENSIONAL FLOW

In the following, superscripts $^{(1)}$ and $^{(2)}$ refer to interfaces 1 (the gas lens) and 2 (location of the sinusoidal interface), respectively. When waves are considered, subscripts $_r$ and $_t$ mean "reflected" and "transmitted." When the geometry is considered, the symbols r and t stand for the distance from the apex of the shock tube and the time, respectively.

A. Wave velocities

In this section, we present the theoretical and expected wave diagram for our experiments.

Let us recall that the gas lens consists in an air-SF_6 interface. Its purpose is to morph the planar incident shock wave into a cylindrical transmitted one. The Mach number of the incident shock wave, $M_i^{(1)}$, is equal to 1.15 in air. The theoretical initial velocity of the transmitted shock wave in SF_6 is equal to $W_t^{(1)} = 165.5$ m/s ($M_t^{(1)} = 1.226$). The cylindrical shock wave is plainly formed at $r = 0.1552$ m. To predict the trajectory, and the strengthening of the imploding shock wave, the Whitham's approximate geometrical theory [31] is used. This theory gives Eq. (3) between the Mach number of the converging shock wave, M, and its area, $\mathcal{A}$:

$$\frac{M\ dM}{M^2 - 1}\lambda(M) + \frac{d\mathcal{A}}{\mathcal{A}} = 0, \tag{3}$$

where $\lambda(M) = (1 + \frac{2}{\gamma+1}\frac{1-\mu^2}{\mu})\ (1 + 2\mu + \frac{1}{M^2})$, with $\mu^2 = \frac{(\gamma-1)M^2+2}{2\gamma M^2-\gamma+1}$. The second interface is located at $r = 0.1$ m. Equation (3) gives for the shock wave before its impact on the second interface a theoretical velocity equal to $W_t^{(1)}(r = 0.1) = 171$ m/s ($M_t^{(1)} = 1.268$). As the velocity of the shock wave in SF_6 increases from 165.5 m/s to 171 m/s between interfaces 1 and 2, its acceleration is barely noticeable. Once this shock wave reaches the second interface, a shock wave is transmitted in air, and a rarefaction wave is reflected in SF_6. The velocity of the transmitted shock wave is initially equal to $W_t^{(2)}(r = 0.1) = 396$ m/s ($M_t^{(2)} = 1.154$). The head of the rarefaction wave travels back at a velocity equal to $W_r^{(2)}(r = 0.1) = -75.86$ m/s.

B. Analysis of the experimental (r,t) diagrams

We will now explain the discrepancies between the expected wave diagram and the actual experimental results.

The experimental data are obtained from two shots, which are labeled #961 and #962. The initial conditions of these shots (Mach number and gas compositions) were planned to be identical. As far as the shock transit in SF_6 is concerned, the two shots give redundant data. The velocity is quasiconstant. A linear fit of the experimental data gives 166.7 m/s and 168.8 m/s for shots #961 and #962, respectively [Figs. 3(a) and 3(b)]. These values agree with the theoretical velocity which starts from 165.5 m/s at interface 1 to reach 171 m/s at interface 2.

At the second interface, a clear mismatch between experiments and theory occurs regarding the reflected wave. The experimental pressure measurements show that this wave is a reflected shock

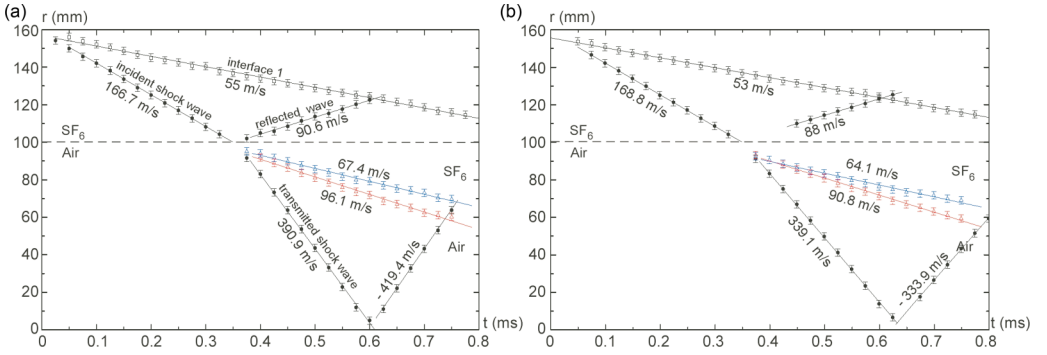

FIG. 3. One-dimensional wave diagrams (r-t plane) reconstructed from pressure measurements, and Schlieren pictures. (a) Shot #961; (b) shot #962.

wave whose velocity is equal to -90.6 m/s and -88 m/s for shots #961 and #962, respectively (linear fits of experimental data). Yet theory predicts a rarefaction wave! This discrepancy is explained by the presence of the grid bars. Indeed, they generate a reflected shock wave (see Appendix A). The trajectory of this shock wave can be theoretically estimated. It is in reasonable agreement with the experimental data: at $t = 0.6$ ms, the location of the shock wave is $r = 0.122$ m in the experiment, and the theory predicts $r = 0.119$ m.

We now focus on the transmitted shock wave in the apex section. The shock wave velocity, $W_t^{(2)}$, and the travel time of the shock wave between interface 2 and the apex, Δt_{focus}, for the two experimental cases are compared with the theoretical values in Table I.

For shot #961, the relative discrepancies between experimental and theoretical data are within the error bar of the experiments. Therefore, we will consider that the gases are pure for shot #961. For shot #962, the velocity of the transmitted shock wave is slower than expected. The relative discrepancy with respect to the theoretical velocity is about 16%. Two reasons can potentially explain this. First, the membrane that is initially held by the grid, and that separates the SF_6 from air, could absorb a part of the incident shock-wave energy. However, if the membrane at the second interface had any influence on the flow, it would have been seen on shot #961 and at interface 1. Therefore, we dismiss this hypothesis. Second, the air in the apex section of the shock tube could be polluted by SF_6. The resulting mixture would be heavier than air and the transmitted shock wave slower than expected. An 8.8% at SF_6 polluted air would give the correct value for $W_t^{(2)}$ and Δt_{focus}. For shot #962, we will now consider that the gas in the apex section of the shock tube is a SF_6-air mix. The initial density of this gas is $\rho^0_{\text{Mix}} = 1.633\,\text{kg/m}^3$, its adiabatic coefficient is $\gamma_{\text{Mix}} = 1.307$, and the initial sound speed is $c_{\text{Mix}} = 284.78$ m/s.

The post-shock Atwood numbers are $A^+ = -0.687$ and $A^+ = -0.594$ for shots #961 and #962, respectively. The Atwood number at interface 2 is defined as $A = (\rho_{\text{air}} - \rho_{\text{SF6}})/(\rho_{\text{air}} + \rho_{\text{SF6}})$.

Figures 4 and 5 present the theoretical and experimental wave (r,t) diagrams for the two shots.

To further assess our previous conclusions about the composition of the gases, numerical simulations have been performed with the multimaterial arbitrary Lagrangian Eulerian (ALE) package

TABLE I. Velocity, $W_t^{(2)}$, of the transmitted shock wave at the interface 2, and time lapse, Δt_{focus}, between the shock passage at interface 2, and its focusing at the apex.

	Shot #961	Shot #962	Theory (pure gases)	Theory (polluted air)
$W_t^{(2)}$ (m/s)	390.9	333.8	396.1	334.
Δt_{focus} (ms)	0.238	0.280	0.234	0.277

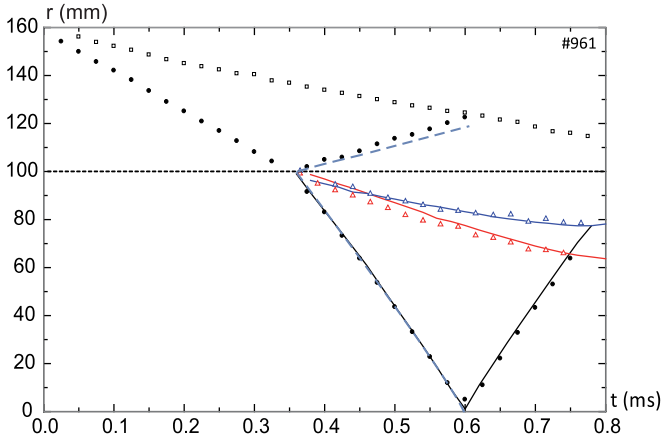

FIG. 4. (r,t) diagram for shot #961. Symbols represent experimental data. Full and dashed lines are from simulation and theoretical results, respectively.

of the Hesione code [32,33]. The subsequent wave trajectories are also presented in Figs. 4 and 5. They match the experiments. Since the code and theory do not take into account the membrane, these comparisons demonstrate that the membranes have no measurable influence on the wave dynamics.

IV. SHAPE OF THE PERTURBATION AT THE SECOND INTERFACE

A. Grid imprint

In this section, we focus on the shape of the distorted interface. Pure gases are considered unless otherwise specified. The bars of the grid materializing the gas lens (interface 1) are not considered since they do not influence the circular converging shock wave in SF_6 [24,25]. As seen in Fig. 2, the perturbation on the second interface, 2, develops a sawtooth shape. This is not what is expected from the growth of a single-mode bidimensional (2D) sinusoidal initial perturbation. We will show that the grid bars are to be taken into account to explain this peculiar shape of the interface. This inference is established with numerical simulations. To compute the grid bars, the pure Eulerian package of the Hesione code must be used to mesh these stationary areas. This package is a Lagrangian remap

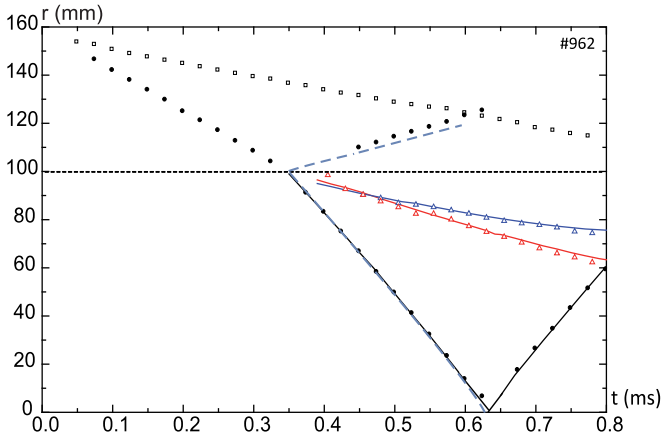

FIG. 5. (r,t) diagram for shot #962. Symbols represent experimental data. Full and dashed lines are from simulation and theoretical results, respectively.

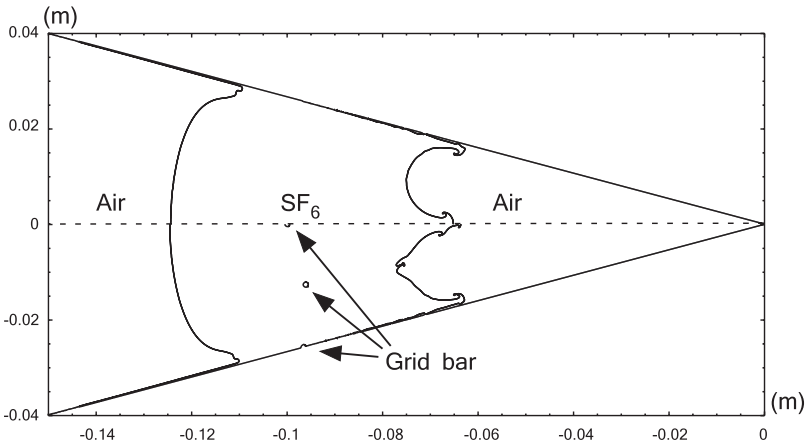

FIG. 6. 2D numerical simulations. Interface shapes shortly before the reshock of interface 2. Top: without the grid bars. Bottom: with the grid bars at the interface 2.

multimaterial hydrocode using a cartesian grid and a BBC scheme [34] with a spatially staggered method. The multimaterial processing is taken into account during the remap step with the Youngs' interface tracking method [35]. A cartesian mesh is used here, and the tilted walls of the convergent shock tube are modeled as staircases. This artificial roughness of the walls generates a numerical boundary layer. However, as our mesh is fine enough, the effect of this boundary layer is negligible.

The azimuthal bars and the crossbars of the grid introduce tridimensional (3D) features in the otherwise 2D geometry of the experiment. Tridimensional Hesione simulations show that the main

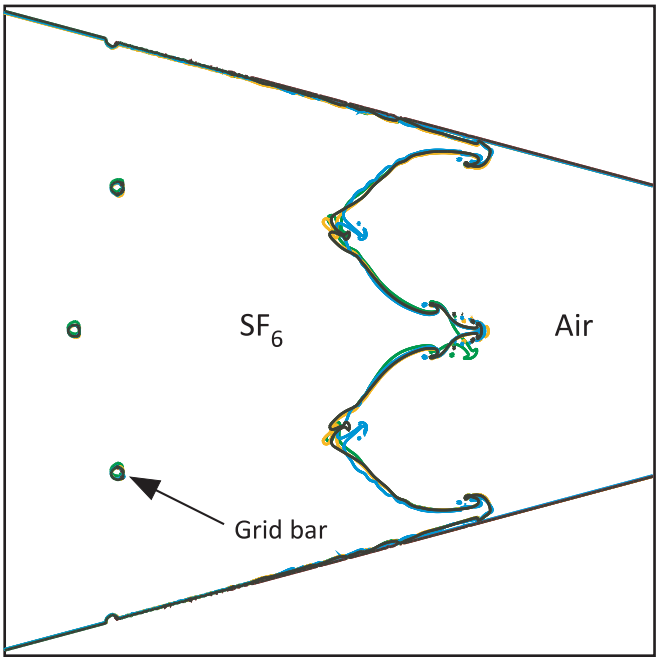

FIG. 7. Numerical simulations. Interface shapes shortly before the interface 2 reshock time. Black, blue, orange, and green shapes are results from numerical simulation with 205, 206, 307 ppw, and 205 ppw with a $\Delta y = +0.3$ mm shifted interface, respectively.

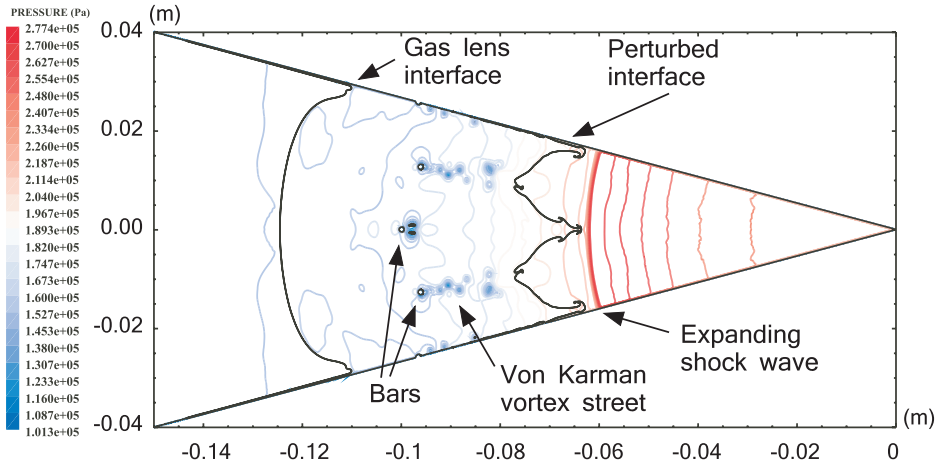

FIG. 8. Numerical simulation of shot #961. Interface shape and pressure field shortly before the reshock of interface 2 ($t = 0.74$ ms).

3D effects (wakes of the crossbars) are negligible for our study (see Appendix B). As a result, in the rest of the paper, the simulations are 2D. To see how the 2D grid bars modify the growth of the perturbation at interface 2, Eulerian simulations with these bars have been performed (bottom part of Fig. 6). The cell sizes of the mesh are $\Delta x = \Delta y = 1.25\ 10^{-4}$ m. So, 205 points per perturbation wavelength (ppw) are used. Only half of the shock tube is computed here.

Without any bar, the interface displays the common features of a single mode sinusoidal RM instability in the nonlinear regime, i.e., a rounded bubble, and a long jet with a mushroom cap. When the grid is taken into account, the shape of the interface becomes sawtooth like. We emphasize that the initial shape of the interface, either in the simulation or the experiment, is not sawtooth like (see Figs. 1 and 2) but exactly sinusoidal. Furthermore, when the grid is computed, additional small jets are generated at the peak and the valley of the interface. They are the consequence of the wakes of the bars. Afterwards, due to the RM instability, these trailing dents on the interface reverse and turn into small extra jets. The numerical convergence of the Hesione code has been studied through a zoning study. A new grid resolution has been considered: $\Delta x = \Delta y = 8.33\ 10^{-5}$ m (307 ppw). Furthermore, the full width of the shock tube has been computed to suppress any imposed symmetry

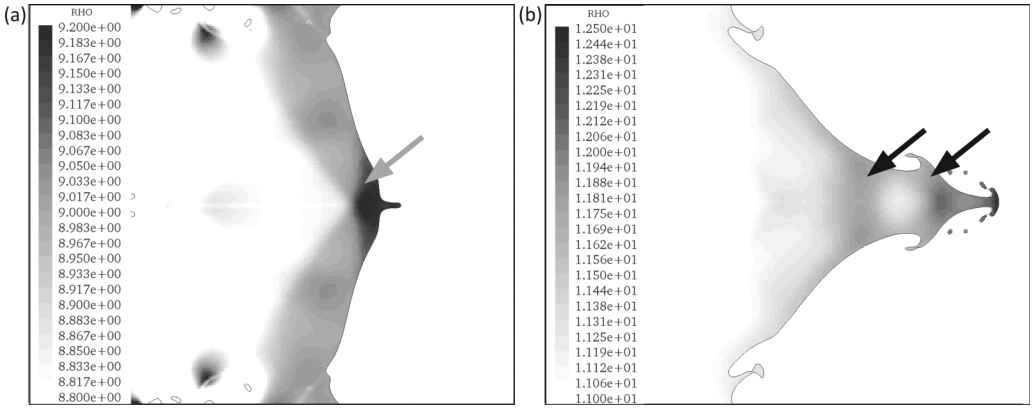

FIG. 9. Numerical simulation of shot #961. Density map near the jet at interface 2. (a) $t = 0.53$ ms. (b) $t = 0.74$ ms.

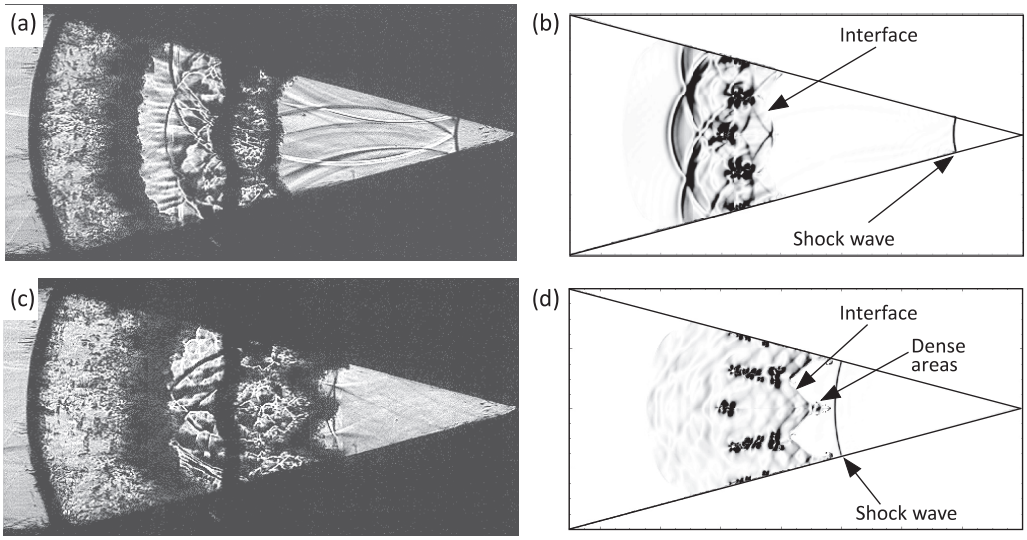

FIG. 10. Shot #961 at $t = 0.53$ ms (top row) and $t = 0.74$ ms (bottom row). (a, c) Experimental pictures. (b, d) Numerical Schlieren pictures.

on the x axis. As shown in Fig. 7, the 205 and 307 ppw interfaces superimpose, with the exception of the additional small jets, which are slightly different.

To check the sensitivity of the flow symmetry to the parity of the number of points, we run a 206 ppw simulation. The results are the same as those obtained from the 205 ppw computation. As a result, we consider that the 205 ppw resolution is fine enough to correctly describe our shock tube. Let us note that the symmetry of the flow with respect to the x axis remains in these simulations, which compute the whole tube. In experiments, it could happen that the stereolithographed grid is slightly out of alignment with respect to the plane of symmetry. To illustrate the sensitivity to such a shifting, we have run a simulation with a $\Delta y = +0.3$ mm shifted interface. This shifting does not change the general shape of the interface. However, the additional small jets are modified, and the one near the x axis now grows downwards (Fig. 7). This result shows that the directions and the amplitudes of the small scale features of the interface are highly sensitive to any offset of the grid.

B. Analysis of the experimental pictures

In this section, by comparing experimental results with numerical simulations, we detail the different contributors to the Schlieren signals and identify the actual location of the interface. The Schlieren technique reveals the density gradients in the flow. Our intent is to track the interface through this means. However, density gradients can have other origins: shock waves, acoustic waves, wakes, and Von Karman vortex streets. These phenomena are exhibited by our numerical simulations as shown in Fig. 8. Another way to create density gradient is through the flow momentum. In our case, the flow field increases the density in the jet vicinity. To illustrate this fact, the Fig. 9 presents the density maps in the jet area at $t = 0.53$ ms and $t = 0.74$ ms. As indicated by arrows in Fig. 9, dense areas can be spotted at the base of the jet. These areas lead to Schlieren shadows, which mingle with the ones that are generated by the interface. Figure 10 presents the experimental pictures and the simulated Schlieren of the corresponding Hesione simulations. The shock waves, the acoustic waves, and the Von Karman vortex streets can be identified. The dense areas at the base of the jets are also tracked by the Schlieren diagnostic and are difficult to separate from the interface signal. We stress that these dense areas are not due to any mixing since the tracking method of the Hesione code keeps the interface as a sharp boundary. In the experiments, the membrane remnants stop

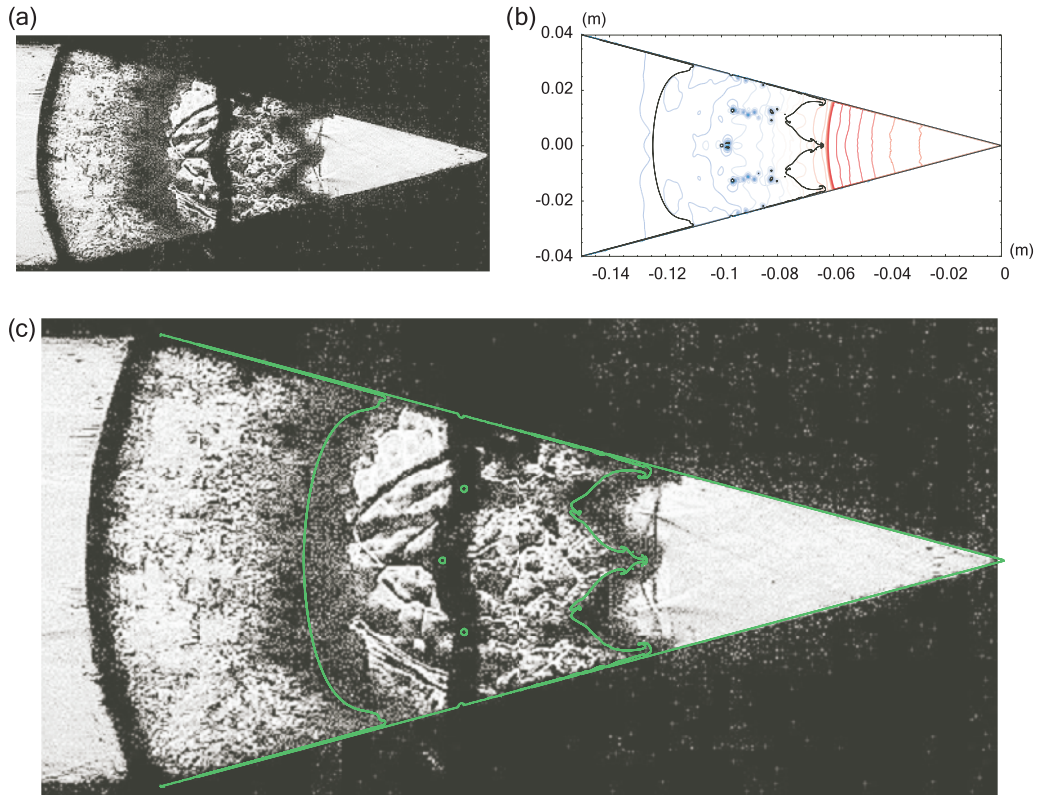

FIG. 11. Shot #961 before the reshock of interface 2 ($t = 0.74$ ms). (a) Experimental picture. (b) Numerical simulation with the interfaces (black lines) and the pressure field (colored contours). (c) Superposition of the experimental image and the numerical interfaces (green).

the light propagation and appear in the pictures. However, they are not computed in the numerical simulations.

Let us now compare the numerical SF_6-air interface with the corresponding experimental photograph for shot #961 (Fig. 11) at $t = 0.74$ ms. We emphasize that both numerical and experimental data are synchronized without any time shifting. At this moment, the numerical and experimental shock waves superimpose [Figs. 11(a) and 11(b)]. On the photograph [Fig. 11(a)], the interface between SF_6 and air is blurred. This foamy zone is partially due to the 3D effects and mainly due to the membrane remnants (see Appendix B). Figure 11(c) shows that the computed interface overlaps the left boundary of the blurred zone. In earlier works [30], we showed that when a shock wave goes from a heavy gas to a light one, the membrane remnants are expelled ahead of the interface. Figure 11(c) confirms our previous assertions: the foamy zone mainly consists of membrane remnants, stays ahead of the SF_6-air interface, and does not reduce the perturbation growth. These results are confirmed by shot #962 (Fig. 12).

The following conclusions can be drawn from the interpretation of the experimental data:

(1) the grid bars change the shape of the perturbation at the interface: at early time, the wake of the crossbars can be seen, but these wakes rapidly fade, and only the 2D bars (along the y axis) have an effect on the perturbation dynamics;

(2) the resulting shape of the interface is sawtooth like, and the 2D numerical simulations match the left boundary of the experimental interfacial area;

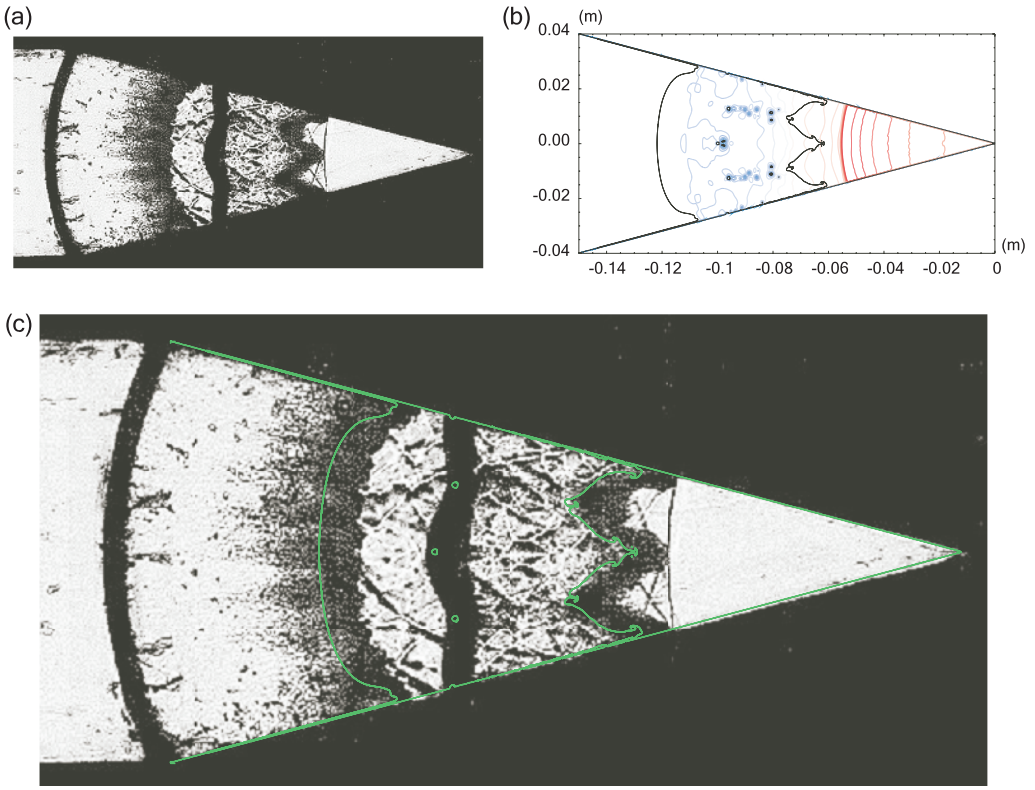

FIG. 12. Shot #962 before the reshock of interface 2 ($t = 0.78$ ms). (a) Experimental picture. (b) Numerical simulation with the interfaces (black lines) and the pressure field (colored contours). (c) Superposition of the experimental image and the numerical interfaces (green).

(3) in the heavy-to-light configuration, the membrane remnants are expelled away from the interface and do not influence its dynamics [27,30];

(4) dense areas at the base of the jet alter the Schlieren picture of the interface.

V. GROWTH OF THE INSTABILITY

The aim of this section is to show that, even if the grid bars induce a change of the interface shape, the growth of the fundamental mode is not modified much. We also characterize the regimes of the instability. As we focus on the interface dynamics, the origin of time is now taken at the moment when the entire interface 2 starts moving. We will denote the time as τ ($\tau = t - 0.36$ ms).

A. Amplitude of the perturbation

Thanks to the previous section, we can depict the experimental interface area as in Fig. 13(a): the left side of the blurred zone matches the 2D interface, and this blurred zone is mainly due to the membrane remnants. Let us denote the locations of the peak and valley of the 2D interface as points A and B and the locations of the peak and valley of the right side limit of the foamy zone as points C and D.

The key data we need to estimate is the amplitude of the 2D interface, which writes as $a(t) = \frac{1}{2}(r_A - r_B)$. Due to the dense areas at the base of the jets, the location r_B of the jet cannot be precisely located in the experiments. However, the trajectories of the other points A, C, and D can be measured

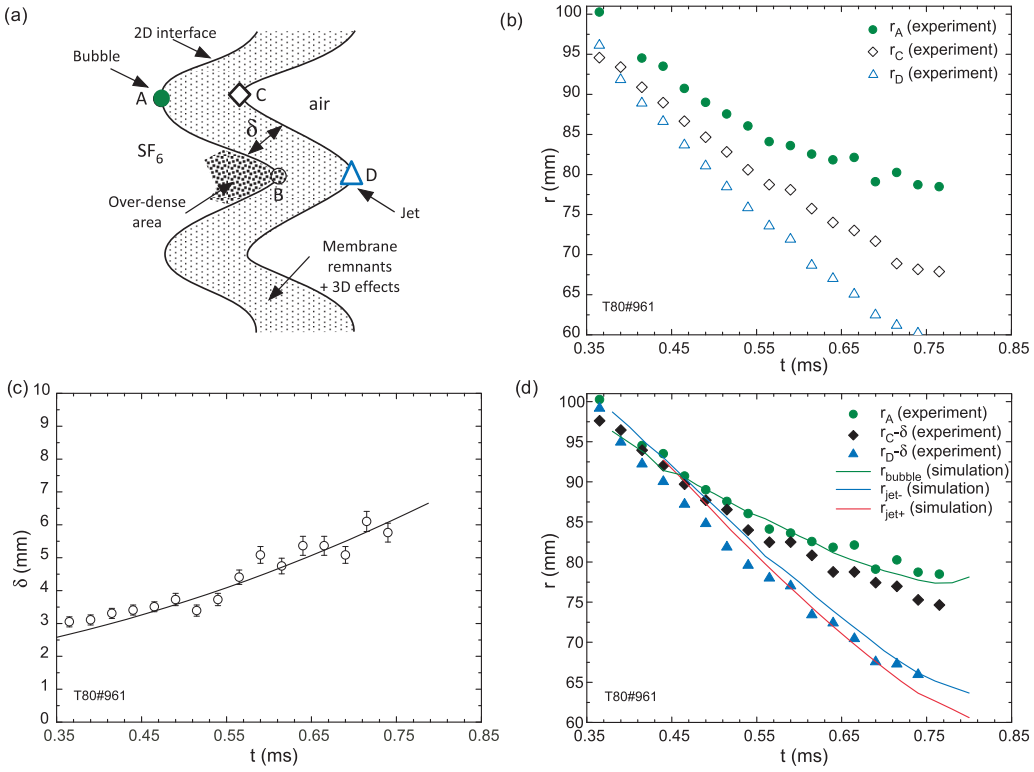

FIG. 13. Interface study for shot #961. (a) Schematic of the Schlieren picture, (b) experimental location for points A, C, D, (c) growth of the foamy zone (the curve is a least-squares fit), (d) comparison between numerical and experimental estimates of the locations of the interface peak and valley. Symbols are obtained from the experiments and Eq. (4). Curves are from the numerical simulations. For the trajectory of the jet, the two curves are obtained by taking into account or not the extra small jet, which is induced by the grid.

[Figs. 13(b) and 14(b)]. Let us note that the width, δ, of the membrane remnant zone grows steadily with time [Figs. 13(c) and 14(c)]. We make the following assumption to estimate the location of point B:

$$r_B \approx r_D - \delta. \tag{4}$$

Figures 13(d) and 14(d) present the trajectories of the peak and valley of the interface for the two shots where the experimental location of the jet, r_B, is computed with Eq. (4). They are compared with two numerical results. The first one is obtained by taking into account the amplitude of the small jet, which appears at the tip of the main jet (marked as "jet+"), and the second one by removing this amplitude (marked as "jet–"). The experimental jet trajectories, which are deduced from the assumption Eq. (4), now follow the numerical ones. Concerning the bubble trajectories, the agreement between experiments and simulations is excellent without any assumption. Let us remark that, as the membrane remnants are not computed by the Hesione code, the good agreement between numerical and experimental trajectories further supports the fact that the interface is unaffected by the membrane remnants in the "heavy-to-light" configuration.

B. Regime of the instability

In the planar geometry, the linear phase of the RM and the RT instabilities is defined by $|k\ a(\tau)| < 1$, where k is the wave number. For the RM instability, this phase is characterized by a perturbation

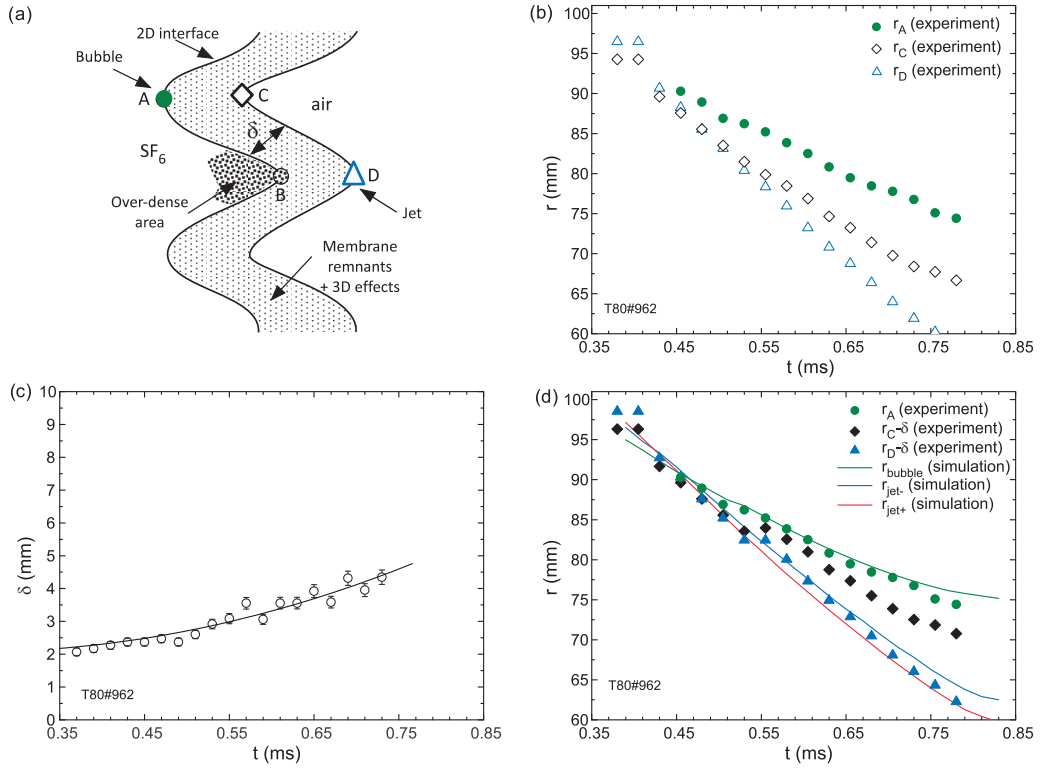

FIG. 14. Interface study for shot #962. (a) Schematic of the Schlieren picture, (b) experimental location for points A, C, D, (c) growth of the foamy zone (the curve is a least-squares fit), (d) comparison between numerical and experimental estimates of the locations of the interface peak and valley. Symbols are obtained from the experiments and Eq. (4). Curves are from the numerical simulations. For the trajectory of the jet, the two curves are obtained by taking into account or not the extra small jet, which is induced by the grid.

growth, which linearly increases over time. In the nonlinear regime, the instability then saturates to a logarithmic growth [36].

In the cylindrical geometry, $k\,a(t)$ is replaced by $n\,a(t)/R$, where n is the mode number of the perturbation, and R is the radius of the unperturbed interface. At first order, the velocity of the interface can be considered as constant and equal to ΔU. As a result, R can be approximated by $R(t) = 0.1 - \Delta U\ t$, with $\Delta U = -82.4$ m/s and -79 m/s for shots #961 and #962, respectively. In our case, n is equal to 24.11. Just before the reshock, $|n\,a/R| \approx 1.52$ for shot #961. We conclude that the instability should be in the nonlinear regime at reshock time. Surprisingly, the growth of the perturbation for shots #961 and #962 seems to linearly depends on time with no saturation (Fig. 15). In the following sections, we investigate and explain this lack of saturation in the nonlinear regime.

C. Influence of the grid

As seen in Appendix B, 3D effects introduce only short-lived small length scale perturbations. Consequently, the left side of the experimental interfacial quickly corresponds to the 2D interface [see Figs. 11(c) and 12(c)], and this will be all the more true in a spectral analysis. To study the influence of the grid bars in the spectral domain, Fourier analyses of the shape of the 2D numerical interface are performed. Figure 16(a) presents, for the conditions of shot #961, the growth of the first three harmonics for simulations with and without the grid bars.

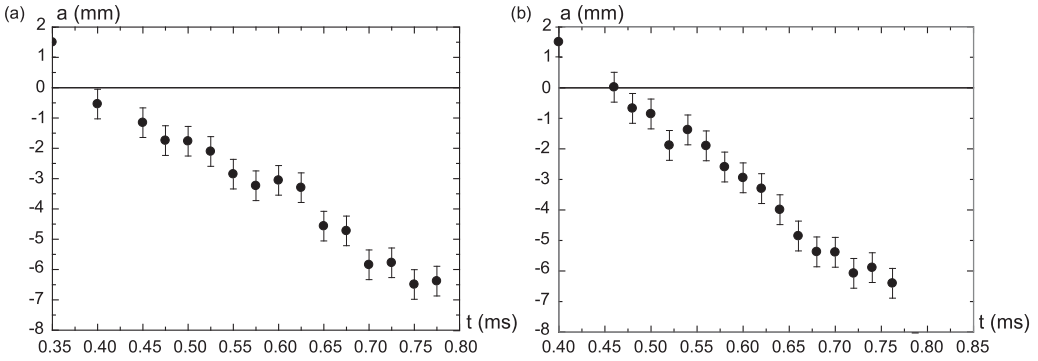

FIG. 15. Amplitude of the perturbation. (a) shot #961. (b) shot #962.

It appears that the growth of the first harmonic with the grid bars is similar to the one without the grid. However, a 14% increase of the growth rate can be noticed due to the grid. This value is constant over time. The influence of the grid appears to be more important on the amplitude, η_2 of the second harmonic. Its amplitude should be negative since the weakly nonlinear theory [37] predicts $\eta_2 = \frac{v_0^2(2\,A\,n-1)\,\tau^2}{4\,r_0^2}$ with $A = -0.687$ and $v_0 = \frac{da}{d\tau}|_{\tau=0}$. But the numerical simulation with the grid shows initially a positive growth. This amplification saturates (around $\tau = 0.08$ ms), and then the expected evolution is recovered with a smaller growth rate than predicted by the theory. The growth of the third harmonic is, as the first one, enhanced by the grid bars. Even if substantial discrepancies exist on the growth rates of the second and third harmonics, the amplitudes of these harmonics remain small in comparison with the amplitude of the first harmonic. As a result, the feedback on the first harmonics stays low. These conclusions are in accordance with the ones which were drawn from a previous study [27] in the planar case: the grid adds short-wavelength (swl) perturbations to the single-mode interface with low feedback on the fundamental mode. Finally, the similar growths of the first harmonic with or without the grid show the lack of saturation of the instability is not due to the grid. Concerning the shape of the interface, this Fourier analysis easily demonstrates how a sawtooth shape is obtained. This is illustrated by a reconstruction of the interface with the first three modes at $\tau = 0.35$ ms [Fig. 16(b)]. Even if at $\tau = 0$ the interfaces with or without the grid are sinusoidal, the small discrepancies between the first three modes are enough to transform a round shape in a sawtooth one.

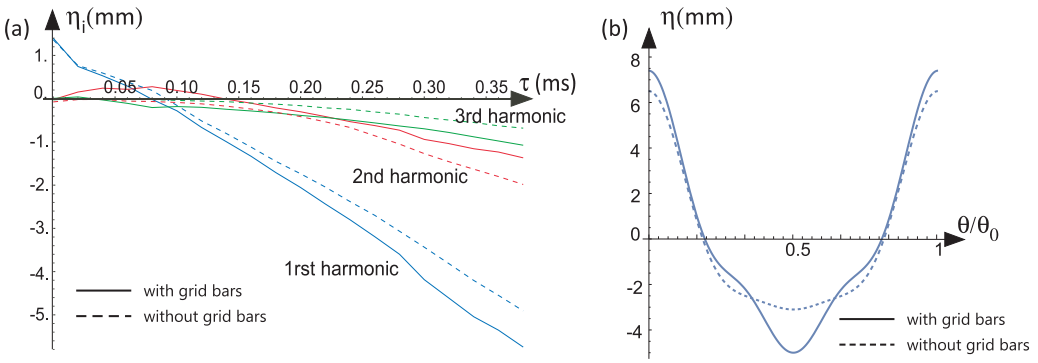

FIG. 16. Analysis of the interface shape for the shot #961. (a) Amplitudes of the first three harmonics. (b) Reconstructed shape at $\tau = 0.35$ ms. Full and dotted curves are obtained from simulations with and without the grid bars, respectively.

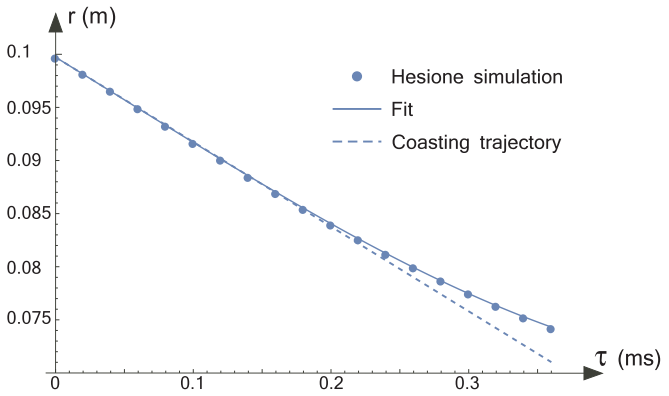

FIG. 17. Trajectory of the unperturbed interface from the Hesione simulation without any grid. Symbols, full and dashed lines represent the raw numerical results, the subsequent fit, and the pure coasting trajectory, respectively.

D. Theoretical modeling

Most theoretical models dealing with the BP effects in cylindrical geometry consider the canonical single-mode problem. It is important to estimate the accuracy of such models either by comparison with experiments or simulations. If a 14% discrepancy on the growth rate is tolerated, our experimental results could be directly used as a reference. However, we choose to use the 2D numerical simulation without the grid to reduce the uncertainties and specifically work on the fundamental mode. The first question is to estimate if our case is a pure RM instability (no post-shock acceleration of the interface). To address it, we have performed a numerical simulation with no perturbation at the SF_6-air interface. It appears that the 1D motion of the interface undergoes a slight deceleration as it travels toward the apex (Fig. 17). This deceleration is due to the pressure gradient, which is generated by the focusing and strengthening shock wave. Consequently, a RT instability is superimposed on the RM instability.

The radius of the unperturbed interface can be fitted by $R(\tau) = 0.0997 - 79.74\ \tau - 16370\ \tau^2 + 1.162\ 10^8\ \tau^3$. At $\tau = 0.35$ ms, the distance from a coasting trajectory is 3 mm, which corresponds to a relative discrepancy for the radius equal to 4%.

The linear growth of a single-mode perturbation due to a RT instability in cylindrical geometry for incompressible fluids has been derived in Ref. [20]. The differential equation for this growth writes as

$$\frac{d^2a}{d\tau^2} + 2\frac{\dot{R}}{R}\frac{da}{d\tau} - (n\ A - 1)\frac{\ddot{R}}{R}\ a = 0, \tag{5}$$

where $n = 2\pi/\theta_0$. This equation is valid in the linear regime, i.e., as long as $|n\ a/R| < 1$. The initial conditions of shot #961 are $n = 24.11$ and $v_0 = -14.7$ m/s. For the RT instability, the Atwood number is $A = (\rho_{SF6} - \rho_{air})/(\rho_{SF6} + \rho_{air}) = 0.687$. The resulting growth, $a(t)$, is presented in Fig. 18.

The linear theory for incompressible fluids deviates from the numerical simulation around $\tau = 0.15$ ms, even if the model should be still valid. Two reasons can be invoked to explain this discrepancy: the compressibility of the fluids and the nonlinear regime of the instability. The effect of compressibility has already been theoretically studied in Refs. [18,19,21] by considering uniform compression rate in each fluid or fixed density profiles. These conditions are not fulfilled in our case, since the implosion is initiated by a collapsing shock wave. Figure 19 compares the radial velocities, which are obtained from the Hesione code with the models using velocity potentials. These models describe continuously converging flows, which are not relevant to our experiments.

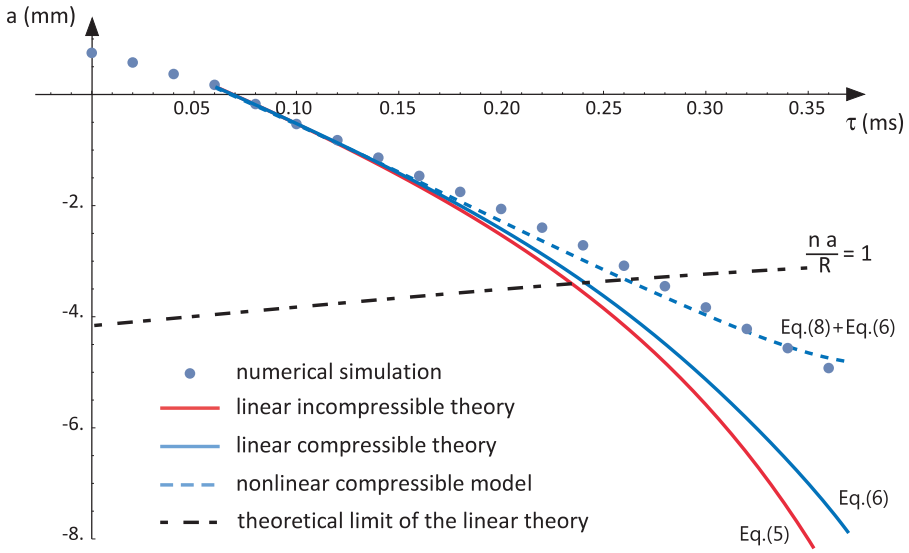

FIG. 18. Growth of the fundamental mode for the initial conditions of shot #961. Symbols are the results obtained from the Hesione code. Red and blue curves are obtained from the linear theories for incompressible and compressible fluids, respectively. The dot curve is obtained from the nonlinear theory with compressible fluids. The dot-dashed line points out the limit of validity of the linear theory.

To estimate the effect of compressibility, we consider time-dependent velocity and density profiles, $v(r,\tau)$ and $\rho(r,\tau)$. Since we want to perform a linear analysis, we only need to know the first-order variation of these profiles at the interface. For the velocity, we write $v(r,\tau) = \dot{R} + \beta(\tau)\,(r - R)$ in each fluid at the interface and derive the resulting linear analysis for the RT instability in the cylindrical geometry. This derivation takes into account the time and spatial variations of the velocity and density at the interface (see Appendix C). The subsequent differential equation for the amplitude of the perturbation writes as

$$\frac{d^2a}{d\tau^2} + C_1(\tau)\frac{\dot{R}}{R}\frac{da}{d\tau} - n\,A(\tau)\frac{\ddot{R}}{R}\,a + C_2(\tau)\frac{\dot{R}^2}{R^2}\,a = 0. \tag{6}$$

The functions $C_1(\tau)$ and $C_2(\tau)$ are displayed in Appendix C. Density and velocity are the main functions that drive Eq. (6).

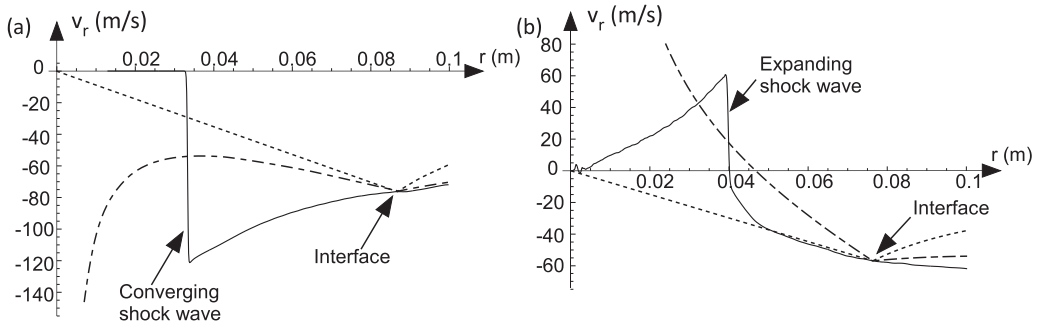

FIG. 19. Radial velocities for shot #961 from the Hesione code (full line), Amendt's [18] (dotted line) and Epstein's [19] (dash-dotted line) velocity potentials. (a) $\tau = 0.16$ ms, (b) $\tau = 0.32$ ms.

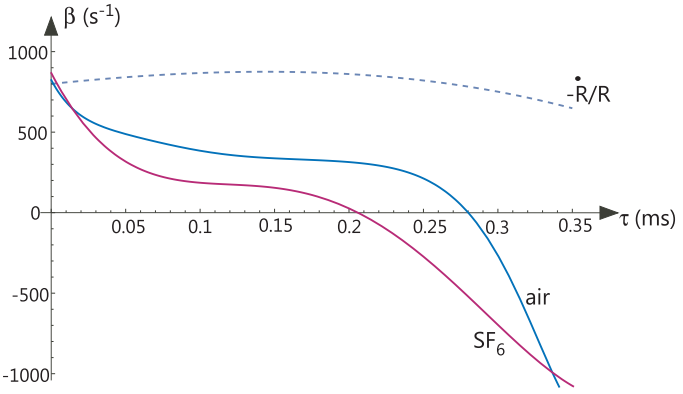

FIG. 20. Parameters β at the interface for SF_6 and air.

(1) In Eq. (6), the densities played a role only through the Atwood number. In the studied case, density of SF_6 and air increases from 8.45 to 11.75 kg/m^3 and from 1.55 to 2 kg/m^3 before the reshock, respectively. However, the time-variation of the Atwood number is small: from 0.687 to 0.706. As a result, the noticeable increase of densities at the interface does not play a significant role in the growth of the perturbation.

(2) Functions $C_1(\tau)$ and $C_2(\tau)$ depend mainly on the velocity parameter β. In our case, the time variation of β is evaluated from the numerical simulation (Fig. 20). From Eq. (6), it can be noticed that if $\beta = -\dot{R}/R$, then Eq. (5) is obtained. This means that if the velocity profile at the interface writes as $v(r,\tau) = \dot{R} - \dot{R}/R\ (r - R)$, then compressible fluids would behave as incompressible ones for the RT instability. In our case, the values of β in SF_6 and air clearly depart from $-\dot{R}/R$ (Fig. 20). The theoretical study of the role of the compressibility through the functions $C_1(\tau)$ and $C_2(\tau)$ or the parameter β is left for future work.

The growth of the perturbation, which is predicted by Eq. (6), is plotted in Fig. 18. Taking into account compressibility slightly reduces the discrepancy between theory and the numerical simulation. Even if the compressibility entails a small effect on the instability in the linear phase, it is important to estimate it because this small effect will modify the initial conditions of the nonlinear phase.

To estimate the effect of nonlinearity, we start from the weakly nonlinear analysis, which is performed in Ref. [23]. This perturbation theory for RT instability in the cylindrical geometry gives

$$\eta_{NL}^{(1)} = \eta_L^{(1)} - \frac{1}{R_0^2}[n^2(3A^2+1) - A\ n - 9]\left(\eta_L^{(1)}\right)^3, \tag{7}$$

where $R_0 = R(0)$ and $\eta^{(1)}$ is the amplitude of the first harmonic. The subscripts NL and L stand for nonlinear and linear, respectively. The radius of convergence of this perturbation theory is small. To go beyond the singularity, it is common to use a continuation method. From Eq. (7), a P_2^0 Padé approximant is built. It reads

$$\eta_{\mathrm{NL}}^{(1)} = \frac{\eta_{\mathrm{L}}^{(1)}}{1 + \frac{1}{R_0^2}[n^2(3A^2+1) - A\ n - 9]\left(\eta_{\mathrm{L}}^{(1)}\right)^2} \tag{8}$$

The range of validity of Eq. (8) is limited since as time tends to infinity, this equation predicts that $\eta_{\mathrm{NL}}^{(1)}$ tends to 0. However, it is sufficient to describe the weakly nonlinear regime of the instability. As seen in Fig. 18, the Padé approximant is in good agreement with the numerical simulation. Let us note that the linear amplitude, η_{L}, which is used to reach such a good alignment, comes from the equation for compressible fluids, Eq. (6). The nonlinear growth begins to deviate from the linear theory around $\tau \approx 0.15$ ms, which corresponds to $|na/R| \approx 0.5$.

To summarize our analysis of the studied RM-RT instability in cylindrical geometry:

(1) from $\tau = 0$ to 0.15 ms, which corresponds to $r/R_0 = 1$ to 0.88 and $|na/r| = 0.17$ to 0.41, the instability is in the linear regime and the compressible effects are negligible. Furthermore, as it is shown by a comparison with pure RM theory, the instability still does not feel any BP effect.

(2) from $\tau = 0.15$, which corresponds to $r/R_0 = 0.88$ and $|na/r| = 0.41$, compressibility must be taken into account. In our SF_6-air configuration, compressibility reduces the growth of the instability. Deceleration of the interface begins to influence the growth rate. The interface dynamics is driven by both RM and RT instabilities.

(3) from $\tau = 0.17$, which corresponds to $r/R_0 = 0.86$ and $|na/r| = 0.47$, the instability is in the nonlinear regime, and even if its effect is small, compressibility must be taken into account.

(4) In cylindrical geometry, and for the studied heavy-to-light configuration, the BP effects (focusing and subsequent compressibility) lead to a quasilinear time variation of the amplitude of the perturbation in the nonlinear regime of the instability (Figs. 15 and 18).

VI. CONCLUDING REMARKS

This study provides an experimental example where the RM instability is modified by convergence effects. By cross-checking experiments and numerical data, we were able to characterize the growth of a single-mode 2D sinusoidal interface in a cylindrical implosion. We showed that the grid and the membrane, which are used to materialize this interface in the shock tube, do not strongly influence the fundamental mode growth. A seemingly linear time-dependent growth of the perturbation at the interface is obtained. Using compressible and weakly nonlinear theories, we showed that this time dependence is the result of the BP effects in the nonlinear regime of the instability. This time dependence is not the result of the classical growth of the RM instability in planar geometry. In our heavy-to-light configuration, the deceleration of the interface destabilizes the instability. The linear time variation of the amplitude of the perturbation can be seen as the nonlinear saturation of an increasingly destabilized interface.

This study highlights some considerations about hydrodynamic instabilities in converging geometry:

(1) The motion of the background flow must be carefully analyzed to check if any deceleration occurs. In our case, the interface is not purely coasting. A slight slowing of the interface led to the disappearance of the expected classical RM logarithmic saturation. Another example of this apparent postponement of the saturation of the RM instability can be found in laser experiments [10].

(2) Equation (8) succeeds to describe the weakly nonlinear growth of the RM+RT instability. However, the range of validity of such a Padé approximant is quite limited. To predict the nonlinear growth of the instability, theories without secular terms are needed. Our data provide a good test case for candidate theories in the weakly nonlinear regime.

(3) To study the BP effects in ICF relevant experiments, the influence of the shock waves on the background flow must be taken into account. Collapsing shock waves generate a specific velocity field and stratified fluids in their wake. If velocity potentials are to be used to study the convergent RT instability seeded by RM instability, they must adequately describe such a flow. This study has shown that the spatial slope of the velocity at the interface, $\beta(t)$, influences the growth of the instability. With a relevant velocity potential, Eq. (6) will be a useful tool to theoretically study when compressibility comes into play.

ACKNOWLEDGMENTS

The authors are grateful to A. Tortel and M. Bonnefille for their help with the 3D computations. This work is supported by CEA, DAM under Contracts No. 13-31-C-DSPG/CAJ and No. 14-48-C-DSPG/CAJ.

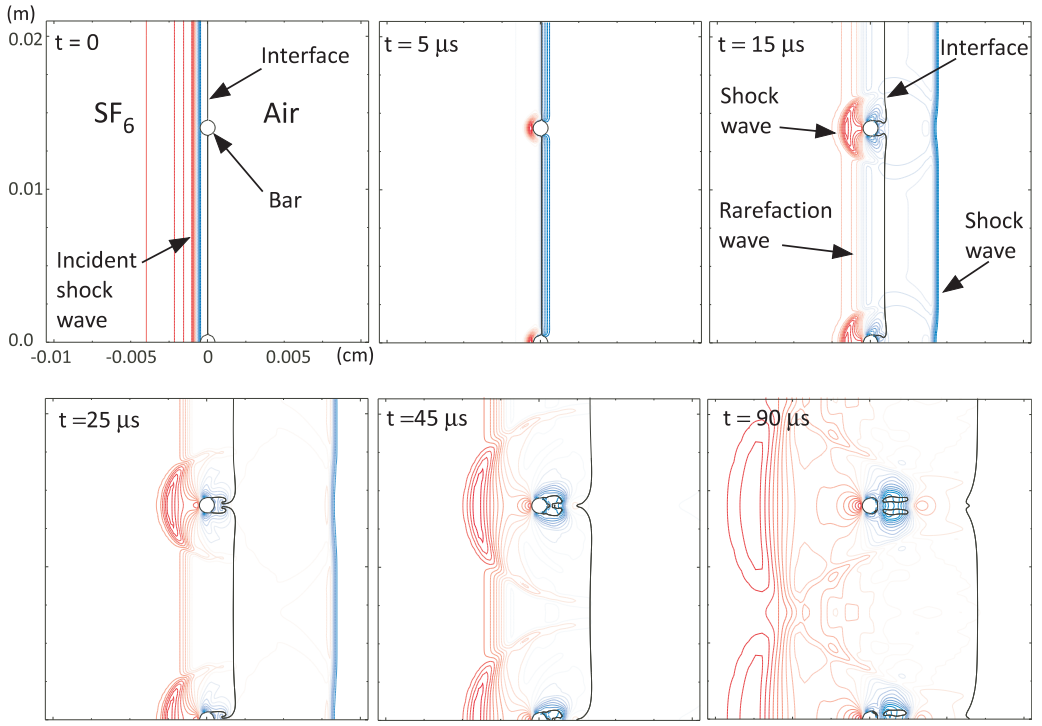

FIG. 21. Interaction between a planar shock wave, an interface SF_6-air, and the grid bars.

APPENDIX A: THE ONSET OF A REFLECTED SHOCK WAVE AT INTERFACE 2

To explain the onset of a reflected shock wave at the second interface, the grid that holds the nitrocellulosic membrane must be taken into account. The bars of the grid are seen by the incident shock wave as an immovable wall. As a result, the shock wave locally bounces back on the bars. In between, normal refraction occurs. When the expanding shock waves have filled the gap between bars, they coalesce. The resulting shock wave is centered on the apex, and its velocity stabilizes.

To assess our conclusions, eulerian numerical simulations with the Hesione code were run in 2D planar geometry. These numerical simulations are solely devoted to the shock-interface interaction in the presence of bars. As seen in Fig. 21, at $t = 5$ μs, high-pressure areas are created on the bars. For approximatively 90 μs, the resulting shock waves expand. Afterwards, they coalesce in a single wave.

The velocity of the final reflected shock wave can be estimated. First, the velocity of the rebounding shock waves on the grid is computed from Ref. [31]. It is equal to 111.9 m/s. The bars of the grid are cylinders with diameter $\Phi_{\text{bar}} = 1$ mm. The reflection of the shock wave on the bars generates a cylindrical high-pressure area around each bar. As a consequence, the interaction between the shock wave and the grid creates an array of cylindrical expanding shock waves, which are centered on each bar. Their initial diameters are equal to Φ_{bar}. We note, r_{local}, the radius of each shock wave centered on each bar. Following Whitham and Guderley [31,38], we can estimate the trajectory, $r_{\text{local}}(t)$, of an expanding shock wave:

$$r_{\text{local}}(t) = (C\ t)^n, \tag{A1}$$

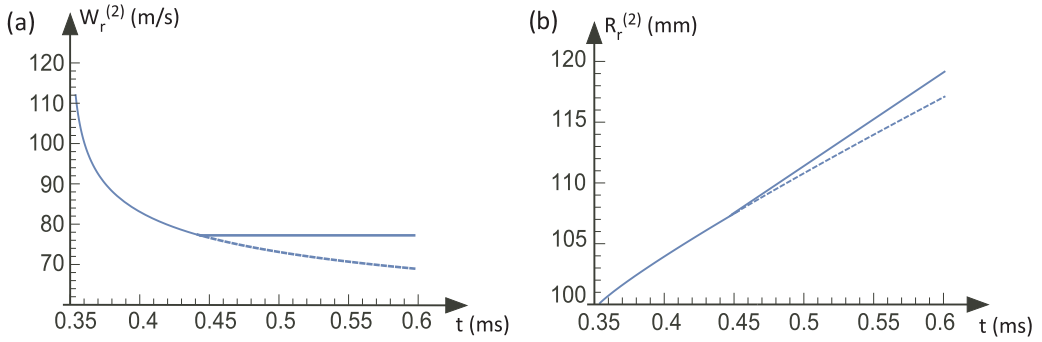

FIG. 22. Reflected shock wave on the grid bar at interface 2. (a) Velocity. (b) Trajectory. Full and dashed lines represent the expansion and the coalescence phases, respectively.

where $n = \frac{n_c}{1+n_c}$, $n_c = 1 + \frac{2}{\gamma} + \sqrt{\frac{2\gamma}{\gamma-1}}$ [31,39], and C a constant. Here, the origin of time is such that $r_{\text{local}}(t = 0) = 0$. In SF_6, n equals to 0.8858. To compute C, we use the initial conditions:

$$r_{\text{local}}(t_0) = (C\ t_0)^n = \frac{\Phi_{\text{bar}}}{2}$$
$$\dot{r}_{\text{local}}(t_0) = n\ C^n\ t_0^{n-1} = 111.9. \tag{A2}$$

The duration t_0 can be seen as the time that would be needed by a hypothetical cylindrical expanding shock wave generated at $r_{\text{local}} = 0$ to reach $r_{\text{local}} = \Phi_{\text{bar}}/2$. Equations (A2) lead to the following solution: $t_0 = 3.958\ \mu$s and $C = 47.41$. The distance between bars is $d = 1.4$ cm. Going from the local reference frame centered on each bar to the reference frame centered on the apex of the shock tube, we write

$$r_r^{(2)}(t) \approx r_{\text{local}}(t) + 0.1. \tag{A3}$$

The theoretical velocity of the expanding shock wave from the slowdown phase [Eq. (A1)] to the constant velocity phase ($r_{\text{local}} = d/2 \Rightarrow W_r^{(2)} = \dot{r}_r^{(2)} = 77.96$ m/s) is presented on Fig. 22(a) (the origin of time is shifted to correspond to the experiment).

The resulting trajectory, $r_r^{(2)}(t)$, is plotted in Fig. 22(b). It is reasonably comparable with the experimental data: at $t = 0.6$ ms, the radius of the reflected shock wave is estimated at 122 mm in the experiment and 119 mm by the theory. In conclusion, the reflected wave at the second interface is a mix between shock waves at the bar locations and classical rarefaction in between. After expanding, the shock waves eventually coalesce and overtake the rarefaction waves.

APPENDIX B: ASSESSMENT OF THE 3D EFFECTS DUE TO THE GRID

The experiment is designed in the cylindrical geometry: the shock tube and the initial interface are 2D. However, the grid that holds the nitrocellulosic membrane is 3D. The azimuthal curved bars and the junctions with the bars that are along the y axis cannot be taken into account in a 2D geometry. To assess the effects of the 3D parts of the grid on the growth of the initially 2D SF_6-air interface, 3D numerical simulations have been performed with the Hesione code. A single pattern of the grid is considered. Furthermore, as the convergence of the interface is not strong, the simulations are run in the planar geometry. The Mach number of the incident shock wave in SF_6 is 1.268. The wavelength of the perturbation is 2.57 cm, the y span of the 3D computational box is 1.6 cm, and the diameter of the bars is 1 mm. The left side of Fig. 23 presents the 3D motion of the SF_6-air interface.

At $t = 350\ \mu$s, the shock wave hits the grid. At $t = 415\ \mu$s [Fig. 23(a)], the cross-shaped folding that is imparted by the grid on the 2D interface can be seen. Behind the grid, a pocket of air stays in the dead flow, and Von Karman vortex streets develop. At $t = 465\ \mu$s [Fig. 23(b)], a wake that is due

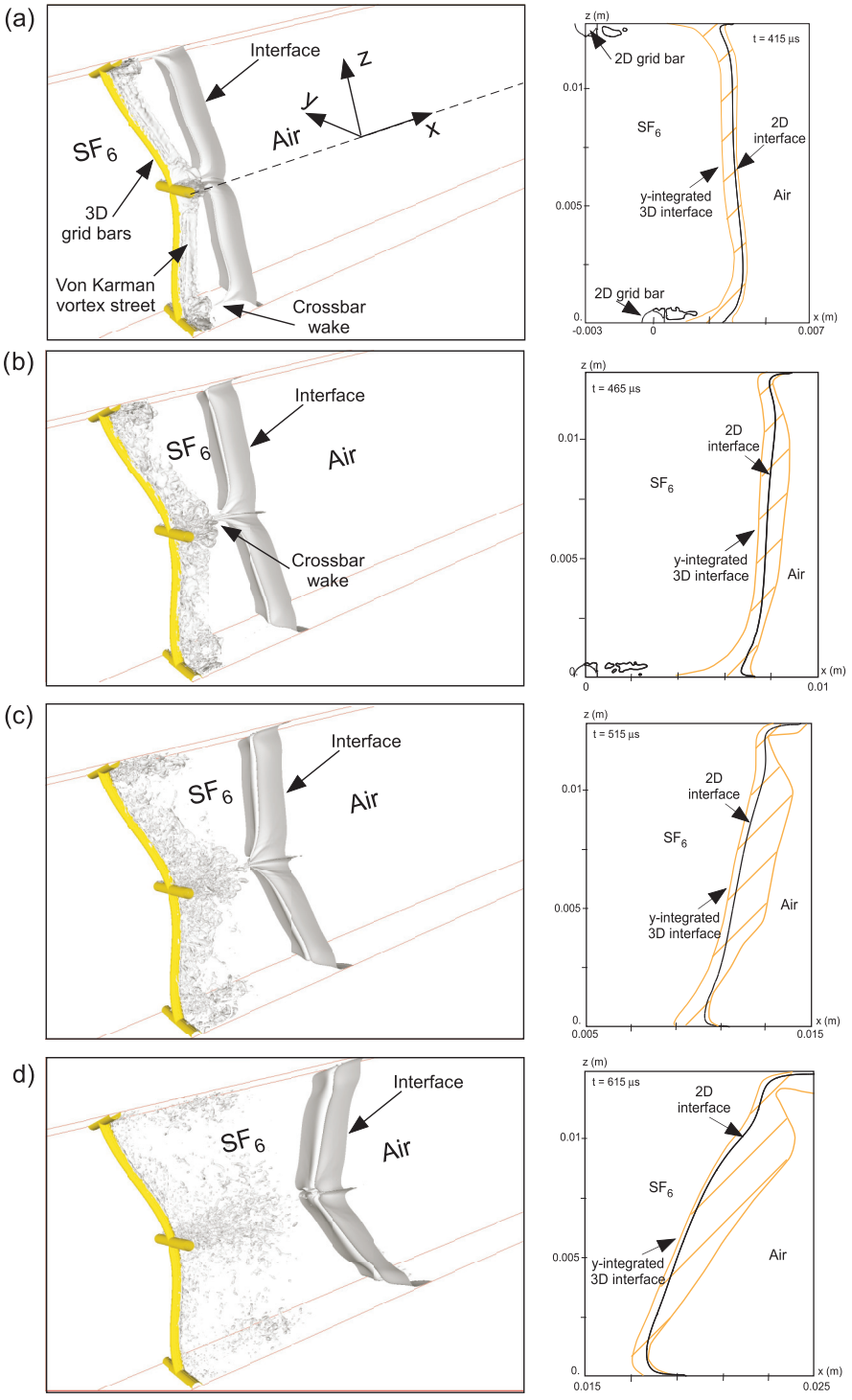

FIG. 23. Tridimensional numerical study of the effects of the grid at t = 415 μs (a), t = 465 μs (b), t = 515 μs (c), and t = 615 μs (d). Left: SF_6-air interface. Right: Comparison between the interface from the 2D simulation and the area of the density gradients in the 3D simulation (upper half of the computational domain).

to the central crossbar can be noticed. This kind of wake can be seen in the experimental pictures at $t = 515\,\mu$s and $t = 590\,\mu$s (Fig. 2). At $t = 515\,\mu$s, the wake has broken up and recedes [Fig. 23(c)]. At $t = 615\,\mu$s, the wake has disappeared, and only the cross-shaped folding remains [Fig. 23(d)]. Let us note that the wakes from the upper and bottom crossbars have already disappeared at $t = 465\,\mu$s since they have been generated earlier. As the experimental Schlieren diagnostic describes a sideview of the density gradients, we now study the density gradients in the simulation. The right-hand side of Fig. 23 displays the span of the area where gradients of density occur in the 3D simulations (dashed area): the density is integrated along the y axis direction, and the edges of the gradient area are determined. We stress that the spreading of this area is not due to mixing. The apparent thickness of the 3D interface is solely due to the sideview of a folded sharp interface. The interface that is obtained from the 2D simulation is superimposed on this area. At $t = 465\,\mu$s, the left boundary of the 3D gradient area has the same shape as the 2D interface with the exception of the crossbar wake on the x axis. This wake recedes with time, and at $t = 615\,\mu$s, the shape of the left boundary of the 3D gradient area matches the 2D interface.

The y-length scale of the wake and the cross-shaped folding is of the same order of the diameter of the bars, i.e., 1 mm. This value is far from the 2D perturbation wavelength of the interface (2.57 cm), and the perturbation that is induced by the bars along the y axis cannot have a strong feedback on the 2D perturbation in the (x-z) plane. As a result, 2D simulations will predict a shape of the interface, which will match the left boundary of the 3D interface either in the spectral domain before $t = 615\,\mu$s and directly after that time. These conclusions are supported by the close match between 2D and 3D at $t = 615\,\mu$s. The x width, δ_{3D}, of the gradient area stays lower than the measured width, δ, of the foamy experimental area [Figs. 13(c) and 14(c)]: $\delta_{3D}(415\ \mu\text{s}) \approx 0.8$ mm, $\delta(415\ \mu\text{s}) \approx 3$ mm, $\delta_{3D}(615\ \mu\text{s}) \approx 2.4$ mm, $\delta(615\ \mu\text{s}) \approx 4.5$ mm. This supports the conclusions of previous works [27,30]: the membrane remnants are the main cause for the spreading of this area and are ahead of the interface in the "heavy-to-light" configuration.

APPENDIX C: LINEAR THEORY FOR THE RT INSTABILITY IN CYLINDRICAL GEOMETRY AND COMPRESSIBLE FLUIDS

The equation of momentum conservation for compressible fluids writes as

$$\frac{\partial \vec{v}}{\partial t} + (\vec{v}.\boldsymbol{\nabla})\vec{v} = -\frac{1}{\rho}\vec{\nabla}P + \vec{g}, \text{ with } \rho(r,t). \tag{C1}$$

For incompressible fluids, $\vec{v} = -\vec{\nabla}\Phi$ and $\Delta\Phi = 0$ gives the form of Φ. For compressible fluids, we can postulate $\vec{v} = -\vec{\nabla}\Phi$, even if the expression for Φ is unknown. However, following Epstein and Amendt [18,19], we can assume that the perturbations are incompressible. As a result, let the potentials for the inner fluid and the outer fluid write as

$$\begin{aligned} \Phi^- &= \Phi_0^- + b_l^-\, r^{-l}\cos(l\theta), \\ \Phi^+ &= \Phi_0^+ + b_l^+\, r^{+l}\cos(l\theta), \end{aligned} \tag{C2}$$

where Φ_0^- and Φ_0^+ are the potentials for the unperturbed flow. For the unperturbed flow, at the interface $\eta = R$, Bernoulli's equations writes as

$$\begin{aligned} \rho_0^-\left(\frac{\partial \Phi_0^-}{\partial t} - \frac{1}{2}\dot{R}^2 - g\eta\right) + P_0^- &= C^- \\ \rho_0^+\left(\frac{\partial \Phi_0^+}{\partial t} - \frac{1}{2}\dot{R}^2 - g\eta\right) + P_0^+ &= C^+. \end{aligned} \tag{C3}$$

We now consider the perturbed flow:

$$\rho^-\left[\frac{\partial\Phi^-}{\partial t}-\frac{1}{2}(v_r^-)^2-g\eta\right]+P_0^-+\delta P^-=C^-$$
$$\rho^+\left[\frac{\partial\Phi^+}{\partial t}-\frac{1}{2}(v_r^+)^2-g\eta\right]+P_0^++\delta P^+=C^+. \tag{C4}$$

We have

$$\begin{aligned} v_r^- &= \dot{R}-lb_l^-\,r^{-l-1}\cos(l\theta),\\ v_r^+ &= \dot{R}+lb_l^+\,r^{+l-1}\cos(l\theta). \end{aligned} \tag{C5}$$

Substituting Eq. (C5) in Eq. (C4), and using Eq. (C3), we linearize the equations, assuming that $\eta=\dot{R}+a\cos(l\theta)$, $a/R\ll 1$, and $\delta P^-=\delta P^+$ at the interface:

$$\rho_0^-(t)(\dot{b}_l^-r^{-l}+\dot{R}\;l\;b_l^-r^{-l-1}-g\;a)=\rho_0^+(t)(\dot{b}_l^+r^{+l}-\dot{R}\;l\;b_l^+r^{+l-1}-g\;a). \tag{C6}$$

Let us now study the equation of motion of the interface.

If an incompressible fluid is considered, following Mikaelian [20], we write $\Phi=-R\dot{R}\,\ln(r)$, $v_r=-\vec{\nabla}\Phi=\dot{R}-\frac{\dot{R}a}{R}\cos(l\theta)$ at the interface. Furthermore, from the definition of η, we also have $v_r=\dot{R}+\dot{a}\,\cos(l\theta)$. Equaling these two expressions for v_r leads to the following differential equations for each fluid:

$$-\frac{\dot{R}a}{R}\pm l\;b_l^{\mp}r^{\mp l-1}=\dot{a}. \tag{C7}$$

For compressible fluids, in the vicinity of the interface, it is always possible to write

$$v_r^{\mp}=\dot{R}+\beta^{\mp}(t)(r-R). \tag{C8}$$

Equating the previous equation with $v_r=\dot{R}+\dot{a}\,\cos(l\theta)$ gives

$$\beta^{\mp}a\pm l\;b_l^{\mp}r^{\mp l-1}=\dot{a}. \tag{C9}$$

If $\beta^{\mp}=-\frac{\dot{R}}{R}$, the equations for compressible fluids are similar to the ones for incompressible fluids. After substitution of Eqs. (C9) in Eq. (C6) and some cumbersome calculations, the following differential equation is obtained for the linear growth of the amplitude $a(t)$:

$$\ddot{a}-l\frac{\ddot{R}a}{R}A(t)+\frac{\dot{a}\dot{R}}{R}C_1(t)-\frac{\dot{R}^2}{R^2}\;a\;C_2(t)=0, \tag{C10}$$

where $C_1(t)=\frac{\rho^+(t)(1-\frac{R}{R}\beta^+)+\rho^-(t)(1-\frac{R}{R}\beta^-)}{\rho^+(t)+\rho^-(t)}$ and $C_2(t)=\frac{\rho^+(t)(\frac{R}{R}\beta^++\frac{R^2}{R^2}\dot{\beta}^+)+\rho^-(t)(\frac{R}{R}\beta^-+\frac{R^2}{R^2}\dot{\beta}^-)}{\rho^+(t)+\rho^-(t)}$.

[1] R. D. Richtmyer, Taylor instability in shock acceleration of compressible fluids, Commun. Pure Appl. Math. **13**, 297 (1960).

[2] E. E. Meshkov, Interface of two gases accelerated by a shock wave, Fluid Dynam. **4**, 101 (1969).

[3] L. Rayleigh, Investigation of the character of the equilibrium of an incompressible heavy fluid of variable density, Proc. London Math. Soc. **s1-14**, 170 (1882).

[4] G. I. Taylor, The instability of liquid surfaces when accelerated in a direction perpendicular to their planes, Proc. R. Soc. London Ser. A **201**, 192 (1950).

[5] G. I. Bell, Taylor instability on cylinders and spheres in small amplitude approximation, Los Alamos Scientific Laboratory Report No. LA-1321, 1951.

[6] M. S. Plesset, On the stability of fluid flows with spherical symmetry, J. Appl. Phys. **25**, 96 (1954).

[7] X. Luo, J. Ding, M. Wang, Z. Zhai, and T. Si, A semi-annular shock tube for studying cylindrically converging Richtmyer-Meshkov instability, Phys. Fluids **27**, 091702 (2015).
[8] D. L. Tubbs *et al.*, Cylindrical implosion experiments using laser direct drive, Phys. Plasmas **6**, 2095 (1999).
[9] S. G. Glendinning *et al.*, Ablation front Rayleigh-Taylor growth experiments in spherically convergent geometry, Phys. Plasmas **7**, 2033 (2000).
[10] J. R. Fincke, N. E. Lanier, S. H. Batha, R. M. Hueckstaedt, G. R. Magelssen, S. D. Rothman, K. W. Parker, and C. J. Horsfield, Postponement of Saturation of the Richtmyer-Meshkov Instability in a Convergent Geometry, Phys. Rev. Lett. **93**, 115003 (2004).
[11] V. A. Smalyuk, D. T. Casey, D. S. Clark, M. J. Edwards, S. W. Haan, A. Hamza, D. E. Hoover, W. W. Hsing, O. Hurricane, J. D. Kilkenny, J. Kroll, O. L. Landen, A. Moore, A. Nikroo, L. Peterson, K. Raman, B. A. Remington, H. F. Robey, S. V. Weber, and K. Widmann, First Measurements of Hydrodynamic Instability growth in Indirectly Driven Implosions at Ignition-Relevant Conditions on the National Ignition Facility, Phys. Rev. Lett. **112**, 185003 (2014).
[12] E. M. Giraldez *et al.*, Machining of two-dimensional sinusoidal defects on ignition-type capsules to study hydrodynamic instability at the National Ignition Facility, Fusion Sci. Tech. **70**, 258 (2016).
[13] K. S. Raman *et al.*, An in-flight radiography platform to measure hydrodynamic instability growth in inertial confinement fusion capsules at the National Ignition Facility, Phys. Plasmas **21**, 072710 (2014).
[14] E. M. Campbell *et al.*, Nova experimental facility, Rev. Sci. Instrum. **57**, 2101 (1986).
[15] T. Boehly *et al.*, Initial performance of the OMEGA laser system, Opt. Commun. **133**, 495 (1997).
[16] G. H. Miller, E. I. Moses, and C. R. Wuest, The National Ignition Facility: enabling fusion ignition for the 21st century, Nucl. Fusion **44**, S228 (2004).
[17] J. L. Peterson, D. T. Casey, O. A. Hurricane, K. S. Ramand, H. F. Robey, and V. A. Smalyuk, Validating hydrodynamic growth in National Igntion Facility implosions, Phys. Plasmas **22**, 056309 (2015).
[18] P. Amendt, J. D. Colvin, J. D. Ramshaw, H. F. Robey, and O. L. Landen, Modified Bell-Plesset effect with compressibility: Application to double-shell ignition target designs, Phys. Plasmas **10**, 820 (2003).
[19] R. Epstein, On the Bell-Plesset effects: The effects of uniform compression and geometrical convergence on the classical Rayleigh-Taylor instability, Phys. Plasmas **11**, 5114 (2004).
[20] K. O. Mikaelian, Rayleigh-Taylor and Richtmyer-Meshkov instabilities and mixing in stratified cylindrical shells, Phys. Fluids **17**, 094105 (2005).
[21] H. Yu and D. Livescu, Rayleigh-Taylor instability in cylindrical geometry with compressible fluids, Phys. Fluids **20**, 104103 (2008).
[22] M. Lombardini and D. I. Pullin, Small-amplitude perturbations in the three-dimensional cylindrical Richtmyer-Meshkov instability, Phys. Fluids **21**, 114103 (2009).
[23] L. F. Wang, J. F. Wu, W. H. Ye, W. Y. Zhang, and X. T. He, Weakly nonlinear incompressible Rayleigh-Taylor instability growth at cylindrically convergent interfaces, Phys. Plasmas **20**, 042708 (2013).
[24] L. Biamino, C. Mariani, G. Jourdan, L. Houas, M. Vandenboomgaerde, and D. Souffland, Planar shock focusing through perfect gas lens: First experimental demonstration, J. Fluids Eng. **136**, 091204 (2014).
[25] L. Biamino, G. Jourdan, C. Mariani, L. Houas, M. Vandenboomgaerde, and D. Souffland, On the possibility of studying the converging Richtmyer-Meshkov instability in a conventional shock tube, Exp. Fluids **56**, 26 (2015).
[26] M. Vandenboomgaerde and C. Aymard, Analytical theory for planar shock focusing through perfect gas lens and shock tube experiment designs, Phys. Fluids **23**, 016101 (2011).
[27] M. Vandenboomgaerde, D. Souffland, C. Mariani, L. Biamino, G. Jourdan, and L. Houas, An experimental and numerical investigation of the dependency on the initial conditions of the Richtmyer-Meshkov instability, Phys. Fluids **26**, 024109 (2014).
[28] G. Fontaine, C. Mariani, S. Martinez, G. Jourdan, L. Houas, M. Vandenboomgaerde, and D. Souffland, An attempt to reduce the membrane effects in Richtmyer-Meshkov instability shock tube experiments, Shock Waves **19**, 285 (2009).
[29] G. Jourdan, L. Houas, L. Schwaederlé, G. Layes, R. Carrey, and F. Diaz, A new variable inclination shock tube for multiple investigations, Shock Waves **13**, 501 (2004).

[30] C. Mariani, M. Vandenboomgaerde, G. Jourdan, D. Souffland, and L. Houas, Investigation of the Richtmyer-Meshkov Instability with Stereolithographed Interfaces, Phys. Rev. Lett. **100**, 254503 (2008).
[31] G. B. Whitham, *Linear and Nonlinear Waves* (Wiley-Interscience, New York, 1974).
[32] D. Eder, K. Koniges, F. Bonneau, J. Vierne, P. Combis, J. Andrews, K. Mann, and B. MacGowan, Simulation of shrapnel to aid in the design of NIF/LMJ target diagnostic configurations, *Proceedings of Inertial Fusion Science and Applications (IFSA'03)* (Elsevier, New York, 2004), pp. 572–575.
[33] F. Bonneau, P. Combis, J. L. Rullier, J. Vierne, B. Bertussi, M. Commandre, L. Gallais, J. Y. Natoli, I. Bertron, F. Malaise, and J. T. Donohue, Numerical simulations for description of UV laser interaction with gold nanoparticles embedded in silica, Appl. Phys. B: Lasers Opt. **78**, 447 (2004).
[34] P. Woodward and Ph. Colella, The numerical simulation of two-dimensional fluid flow with strong shocks, J. Comput. Phys. **54**, 115 (1984).
[35] D. L. Youngs, An interface tracking method for 3D eulerian hydrodynamics code, Tech. Report 44/92/35, AWE, 1984.
[36] K. O. Mikaelian, Explicit expressions for the evolution of single-mode Rayleigh-Taylor and Richtmyer-Meshkov instabilities at arbitrary Atwood numbers, Phys. Rev. E **67**, 026319 (2003).
[37] W. H. Liu, C. P. Yu, W. H. Ye, L. F. Wang, and X. T. He, Nonlinear theory of classical cylindrical Richtmyer-Meshkov instability for arbitrary Atwood numbers, Phys. Plasmas **21**, 062119 (2014).
[38] G. Guderley, Starke kugelige und zylindrische Verdichtungsstöße in der Nähe des Kugelmittelpunker bzw. der Zilinderachse, Luftfahrforschung **19**, 302 (1942).
[39] R. F. Chisnell, The motion of a shock wave in a channel, with applications to cylindrical and spherical shock waves, J. Fluid Mech. **2**, 286 (1957).